The Astronomical Journal, 165:228 (8pp), 2023 June https://doi.org/10.3847/1538-3881/accc30

Dispersion Characteristics of the Multi-mode Fiber-fed VIPA Spectrograph

Xiaoming Zhu[1,2], Dong Lin[1,2,3], Zhongnan Zhang[1,2,3], Xintong Xie[1,2,3], and Jinping He[1,2,4]
[1] Laboratory of Solar and Space Instrument, National Astronomical Observatories / Nanjing Institute of Astronomical Optics & Technology, Chinese Academy of Sciences, Nanjing 210042, People's Republic of China; jphe@niaot.ac.cn
[2] CAS Key Laboratory of Astronomical Optics & Technology, Nanjing Institute of Astronomical Optics & Technology, Chinese Academy of Sciences, Nanjing 210042, People's Republic of China
[3] University of Chinese Academy of Sciences, Beijing 100049, People's Republic of China
[4] University of Chinese Academy of Sciences, Nanjing 211135, People's Republic of China
Received 2022 December 15; revised 2023 March 12; accepted 2023 April 10; published 2023 May 4

Abstract

A high-resolution ($\mathcal{R} > 10^5$), multi-mode fiber-fed spectrograph on large telescopes with a reasonable size is desirable in astronomy. In this work, the dispersion characteristics of a multi-mode fiber-fed Virtually Imaged Phased Array (VIPA) spectrograph are studied theoretically and experimentally. A VIPA spectrograph, fed by multi-mode optical fibers with the operating wavelength at 750 ∼ 770 nm, is designed and built in our laboratory. After calibration with a homemade Yb:fiber ring laser frequency comb (with a repetition frequency of 808 MHz), the measured spectral resolution fed by multi-mode fibers with core diameters $\varnothing$ = 10, 25, 50, and 105 μm is comparable with that of the single-mode fiber, i.e., $\mathcal{R} = 7.62 \times 10^5 \sim 8.97 \times 10^5$, with equivalent transmission efficiencies. This verifies experimentally that the spectral resolution is much less affected by the core diameters of the input fibers when compared with that of échelle spectrographs. It is also found that the diffraction envelope of the VIPA spectrograph relies on the coherence of light sources and the width of the point-spread function is inversely proportional to the spatial position on the detector. Since the VIPA spectrograph has no imaging process in the main dispersion direction, the spectral resolution is insensitive to the width of the input slit or the fiber diameter. This makes the VIPA spectrograph a promising instrument to attain an ultra-high spectral resolution ($\mathcal{R} > 3 \times 10^5$) on very large telescopes.

Unified Astronomy Thesaurus concepts: High resolution spectroscopy (2096); Astronomical methods (1043); Astronomical instrumentation (799); Astronomical techniques (1684)

1. Introduction

High-resolution spectroscopy is one of the most powerful tools in astronomical observations and has been extensively applied in studies of the chemical abundances of stars (e.g., Monroe et al. 2013), isotopic ratios of galaxies (e.g., Lauroesch et al. 2000; Knauth et al. 2003), as well as the detection of exoplanets (e.g., Anglada-Escudé et al. 2016). In recent years, the search for terrestrial planets (and their characterization) in the habitable zone of their parent stars has become an exciting topic in astronomy. However, this requires us to observe fainter objects with high-resolution spectrographs possessing higher precision and with longer temporal stability. To achieve these goals, larger telescopes (10 m class) and observation instruments that are stable over a long period of time are indispensable.

Most of high-resolution spectrographs adopt échelles as the major dispersion element, whose scaling of spectral resolution depends on the telescope diameter according to the Lagrange invariance at seeing-limited conditions (e.g., Schroeder 2000; Ben-Ami et al. 2018); namely, larger telescopes require larger format instruments to achieve high resolution—e.g., ESPRESSO on VLT ($\mathcal{R} \approx$ 190,000) uses a mosaic of three gratings with a dimension of 120 × 20 cm—, which enhances the complexity and cost of bespoke large optics. However, high-resolution spectrographs on larger telescopes (e.g., the Extremely Large Telescope; ELT) might be unrealistic for the detection of O_2 in the transmission spectrum of an Earth-like planet at $\mathcal{R} \sim 3$–5×10^5 (Ben-Ami et al. 2018; López-Morales et al. 2019).

Pupil slicing (e.g., Conconi et al. 2013; Seifahrt et al. 2016) and adaptive optics (e.g., Bechter et al. 2016; Crepp et al. 2016; Jovanovic et al. 2016) are two viable approaches to allow échelle spectrographs to attain a higher resolution on larger telescopes with a reasonable instrument size. However, new dispersion devices based on the interference principle—such as externally dispersed interferometry (EDI e.g., Muirhead et al. 2011; Erskine et al. 2016), Fabry–Perot Interferometer Arrays (e.g., Ben-Ami et al. 2018), and Virtually Imaged Phased Array (VIPA e.g., Bourdarot et al. 2017, 2018; Zhu et al. 2020)—have been proposed to constitute compact instruments with a high spectral resolution for astronomical observations.

The VIPA offers excellent angular dispersion, structural simplicity, low price, and size compactness, and has therefore been widely utilized as a dispersion instrument in communications, biology, and medicine (e.g., Shirasaki 1996; Diddams et al. 2007; Fiore et al. 2016). Recently, there have also been some exploratory studies in astronomy (e.g., Bourdarot et al. 2018; Zhu et al. 2020; Carlotti et al. 2022). Considering that almost all of the current VIPA spectrographs are designed and operated under the diffraction-limited condition, the development of a multi-mode fiber-fed VIPA spectrograph on ground-based telescopes that works on the seeing-limited condition is imperative. Zhu et al. (2020) have studied the dispersion characteristics of a single-mode fiber-fed VIPA spectrograph, which leaves the more important multi-mode fiber-fed spectrograph as an open question. In this work, we investigate

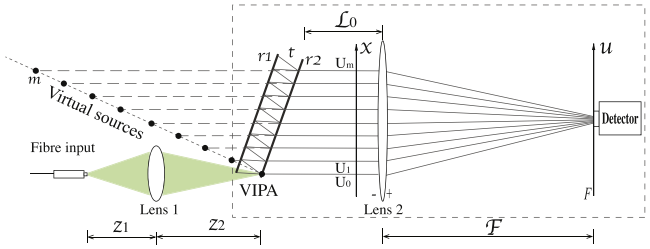

Figure 1. The spectral dispersion principle of the VIPA.

the features of multi-mode fiber-fed VIPA spectrographs, both theoretically and experimentally, by comparing with those of the single-mode fiber input. Thanks to the absence of an imaging process, as well as the mutual restriction between the échelle spectral resolution and the telescope aperture, the VIPA spectrograph is particularly suitable for utilization on large telescopes.

This paper is organized as follows. The VIPA dispersion principle is discussed theoretically with the plane-by-plane approach in Section 2. Section 3 describes the experimental studies of the dispersion characteristics of the VIPA spectrograph, such as spectral resolution, diffraction envelope, and point-spread function. This section will also investigate the *A*-band oxygen absorption lines to verify the spectral resolution of the VIPA spectrograph. Finally, the discussion and conclusions are given in Section 4.

2. Theoretical Analysis

The VIPA as a dispersion element is analogous to the modified Fabry–Perot etalon in structure, although there are differences in usage. Figure 1 shows the spectral dispersion principle of the VIPA, in which the signal from the light source is converged by Lens 1 with a focal length f, and travels into the spectrograph via fibers (the multi-mode fiber in normal in astronomical spectrographs). The VIPA is coated with a high-reflective dielectric with a reflectivity r_1 on the front side and a partially-reflective dielectric with a reflectivity r_2 on the rear side. After entering the VIPA, the light undergoes multiple reflections between the two sides and the transmitted light from the rear side splits into many rays. The parallel rays interfere with each other forming distinct output angles dependent on their wavelengths, which can be viewed as the result of the array of virtual light sources in front of of the VIPA. Spherical Lens 2 with a focal length of F is placed at a distance $\mathcal{L}_0$ to the VIPA. The detector is placed at the the focal plane of this lens.

According to the classical lens law of geometrical optics, a real spot image of the fiber section with magnification $M = |\frac{z2}{z1}|$ is formed on the rear side of the VIPA if the condition $\frac{1}{z1} + \frac{1}{z2} = \frac{1}{f}$ is fulfilled. The m-th virtual light source with a dimension of $M \cdot \varnothing_f$ ($\varnothing_f$ is the core size of the fiber in diameter) locates at $x = X_m$ separated by a distance Z_m from Lens 2 with

$$\begin{aligned} X_m &= 2mt \tan\theta_{\rm in} \cos\theta, \\ Z_m &= 2mn_r t/\cos\theta_{\rm in} - 2mt \tan\theta_{\rm in} \sin\theta + L_0, \\ &= 2mn_r t \cos\theta_{\rm in} + L_0, \end{aligned} \tag{1}$$

where n_r and t are the refraction index and the thickness of the VIPA, and $\theta_{\rm in}$ and θ are the incident angles inside and outside of the VIPA, respectively.

Many scientists have derived the dispersion law of the VIPA based on either paraxial or plane wave theory by assuming coherent light sources (e.g., Xiao et al. 2004; Hu et al. 2015). Here, we use the optical diffraction theory instead and calculate the complex amplitudes successively plane by plane within the four planes of interest (source "0," before the lens 2 "−," after the lens 2 "+" and the focal plane "*F*"). Let $U_0(x)$ represent the amplitude and phase distribution across the fiber section, with $U_m(x)$ denoting those of the m-th virtual source. The source field $U_0(x)$ can be either a Gaussian function for a single-mode fiber input or a complicated form for incoherent light with a multi-mode fiber input.

Based on the paraxial approximation, the complex amplitude prior to Lens 2 is given by

$$\begin{aligned} U_{-,m}(x) \propto (r_1 r_2)^m e^{ikZ_m} U_0(x) \\ \otimes \left\{ \frac{1}{i\lambda Z_m} \exp\left[\frac{i\pi (x - X_m)^2}{\lambda Z_m} \right] \right\}, \end{aligned} \tag{2}$$

where the symbol ⊗stands for the convolution operation. After passing through Lens 2, the field distribution becomes

$$U_{+,m}(x) = U_{-,m}(x) \exp\left[-i\frac{k}{2F} x^2 \right]. \tag{3}$$

Finally, the field in the focal plane due to the Fresnel diffraction accounting for the propagation over a distance F can be written as

$$\begin{aligned} U_{F,m}(u) &= e^{ikF} U_{+,m}(x) \otimes \left\{ \frac{1}{i\lambda F} \exp\left(\frac{ikx^2}{2F} \right) \right\} \\ &= \frac{e^{ikF}}{i\lambda F} e^{i\frac{ku^2}{2F}} \mathcal{F}[U_{-,m}(x)]_{u=\frac{x}{\lambda F}} \\ &= (r_1 r_2)^m \frac{e^{ikZ_m}}{\lambda^2 Z_m F} e^{i\frac{ku^2}{2F}} \mathcal{F}[U_{0,m}(x)]_{u=\frac{x}{\lambda F}} \\ &\quad \times \mathcal{F}\left\{ \exp\left[\frac{i\pi (x - X_m)^2}{\lambda Z_m} \right] \right\}_{u=\frac{x}{\lambda F}} \\ &\propto \tilde{U}_0(u) \cdot (r_1 r_2)^m e^{i\frac{ku^2}{2F}} \cdot e^{ikZ_m} \\ &\quad \times \exp\left(-ik\frac{X_m}{F} u - ik\frac{Z_m}{2F^2} u^2 \right). \end{aligned} \tag{4}$$

By substituting Equation (1) into Equation (4), we obtain the optical path difference between two virtual light sources

$$\xi = 2n_r t \cos\theta_{\rm in} - 2t \tan\theta_{\rm in} \cos\theta \frac{u}{F} - n_r t \cos\theta_{\rm in} \frac{u^2}{F^2}. \tag{5}$$

The total field in the focal plane is then given by

$$U_F(u) \propto \tilde{U}_0(u) \cdot \sum_m (r_1 r_2)^m \exp(ikm\xi). \tag{6}$$

Note that the sum in this equation is the Fourier transform of the product of delta functions, namely,

$$A_\delta(u) = \sum_m (r_1 r_2)^m \delta(x - X_m) \delta(z - Z_m), \tag{7}$$

with A_δ depicting the location and intensity of the set of point sources arrayed in the same configuration, such that Equation (6) can be expressed as

$$U_F(u) \propto \tilde{U}_0(u) \cdot \tilde{A}_\delta(u), \tag{8}$$

which has a similar form to the expression of the array theorem in which the interference pattern $U_F(u)$ of an array of similarly oriented identical apertures equals the Fourier transform of an individual aperture function multiplied by the pattern originated from a set of point sources in the same configuration.

The number of the virtual light sources involved in the interference tends to infinity in the case that the transverse aperture of the VIPA is large and the incident angle is small enough. By performing the summation over infinite series, we therefore have

$$\tilde{A}_\delta(u) = \sum_{m=0}^{\infty} (r_1 r_2)^m \exp(ikm\xi) = \frac{1}{1 - r_1 r_2 \exp(ik\xi)}. \quad (9)$$

The intensity distribution in the focal plane is then

$$I_F(u) = |U_F(u)|^2 \propto \frac{\tilde{U_0}^2(u)}{(1 - r_1 r_2)^2 + 4 r_1 r_2 \sin^2(k\xi/2)} \propto \tilde{U_0}^2(u) \frac{1}{1 + P \sin^2(k\xi/2)}, \quad (10)$$

where the parameter P is defined as

$$P = \frac{4 r_1 r_2}{(1 - r_1 r_2)^2}. \quad (11)$$

The first part of Equation (10) is the diffraction envelope of a single source, while the second part is known as the Airy function, which is a periodic function of ξ with the maxima at $\xi_0 = n\lambda_0$ with $n \in \mathbb{Z}$ being the interferential order.

Similar to the derivations in Bailén et al. (2019), the resolving power of the VIPA for the wavelength λ can be obtained as

$$\mathcal{R}_V = \frac{\lambda}{\Delta\lambda} = \frac{\pi}{2} \cdot \frac{\xi}{\lambda} \cdot \sqrt{P}, \quad (12)$$

which indicates that the dispersion ability of the VIPA is related to the refractive index n_r, the thickness t and coating reflectivities $r_{1,2}$ of the VIPA, as well as the geometry of the spectrograph according to Equations (5) and (11).

In our derivations, the irradiance pattern is a set of Airy–Lorentzian interference fringes that are modulated by the diffraction envelope generated by an individual aperture. The dispersion ability of the VIPA is solely determined by the Airy–Lorentzian interference fringes instead of the diffraction envelope according to Equation (10). In the Fabry–Pérot interferometers of post-focus astronomical instrumentation or grating-based spectrographs, the slit/fiber sections image on the focal plane of the imaging lens such that the spectral resolution is restrained by the slit width and the core size of the input fibers. In the setup of the VIPA spectrograph, as shown in Figure 1, the parallel light from the multiple reflections generates an interference pattern through Lens 2 on its focal plane without an object-image correspondence. As a result, the spectral resolution of the VIPA spectrograph is dominated by the resolving power of the VIPA itself instead of the object's dimensions. However, the extended size at the entrance of the VIPA (core diameter of MMFs in our cases) will bring a small shift in the angle of incidence, which will cause a less negligible reduction in resolution than it appears in Equation (12). We will analyze and discuss this point it in detail in Sections 3.2 and 3.4.

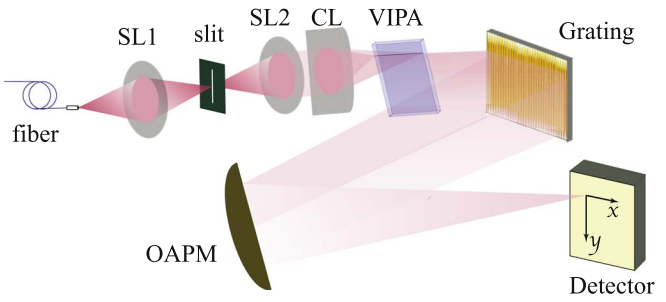

Figure 2. Schematic of the VIPA spectrograph. On the detector, x and y are the dispersion directions of the grating and the VIPA, respectively.

3. Experimental Verification

3.1. Experimental Setup

A fiber-fed VIPA spectrograph, with the schematic shown in Figure 2, is designed to verify our theoretical analysis in Section 2. This spectrograph utilizes a VIPA and an échelle grating as the main and orthogonal dispersion elements, respectively. To demonstrate the resolution of a VIPA spectrograph independent of the fiber diameters, we use various fibers—including the single-mode fiber (SMF, $\varnothing \sim 5$ μm), multi-mode fibers (MMFs) with $\varnothing = 10, 25, 50, 105$ μm, and the octagonal fiber (OF, $\varnothing \sim 100$ μm)—as the input to the spectrograph. A bi-convex lens SL1 with focal length of 25.4 mm is deployed and a 5 μm slit is placed parallel to the dispersion direction of the VIPA at the image spot to guarantee the diffraction-limited sources in the orthogonal direction. This design eliminates the influence of the grating dispersion characteristics.

The VIPA in the operational spectrograph purchased from LightMachinery Inc. (2020) has a volume of $22 \times 24 \times 3.371$ mm^3 filled with fused silica ($n_r \approx 1.46$). The reflectivities are, respectively, $r_1^2 \approx 99.3\%$ and $r_2^2 \approx 98.3\%$ at the working wavelength of 760 nm, providing a theoretical maximal transmission of 71.2%. In the experiments, the focal lengths of the spherical (SL2) and the cylindrical (CL) lens were chosen so that the VIPA transmission efficiencies are as high as possible and have equivalent values for each input fiber to minimize the disturbance of the spectral resolution. Practically, the focal lengths of SL2 and CL are 50 mm and 100 mm, respectively.

An off-the-shelf échelle grating (316 grooves/mm, 63° blaze, 50 mm × 25 mm) is mounted orthogonally to the dispersion direction of the VIPA to separate the dispersion orders. The angle of incidence is roughly 2°.0 for the VIPA and ~70° for the échelle grating. In addition, an off-axis parabolic mirror (OAPM) with an effective focal length of 310.1 mm functions as the focusing mirror and a Thorlabs 8051M-USB CCD camera is placed at the focus of the OAPM to receive the signals without external cooling. We selected the seventh order of the échelle grating, which covers the free spectral range of around 108 nm. The operating wavelength range of the VIPA spectrograph was chosen at 750 ~ 770 nm, based on the requirements of our experiments.

The laser frequency comb (LFC) is a perfect light source for calibrations of the spectral resolution because it possesses an extremely stable and accurate $f_{\rm rep}$, and nearly single-frequency comb teeth (<10 kHz). In our spectrograph, a homemade Yb: fiber ring LFC with a repetition frequency ($f_{\rm rep}$) ~ 808 MHz, corresponding to ~1.56 picometer (pm) at 760 nm (Jiang et al.

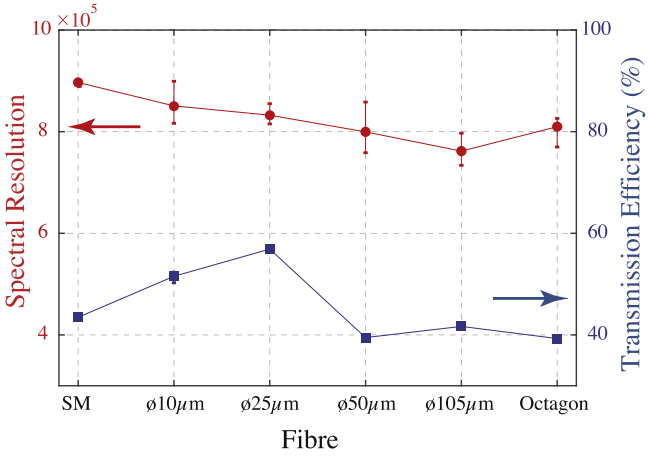

Figure 3. The spectral resolution and the total transmission efficiency of the VIPA with different kinds of input fibers.

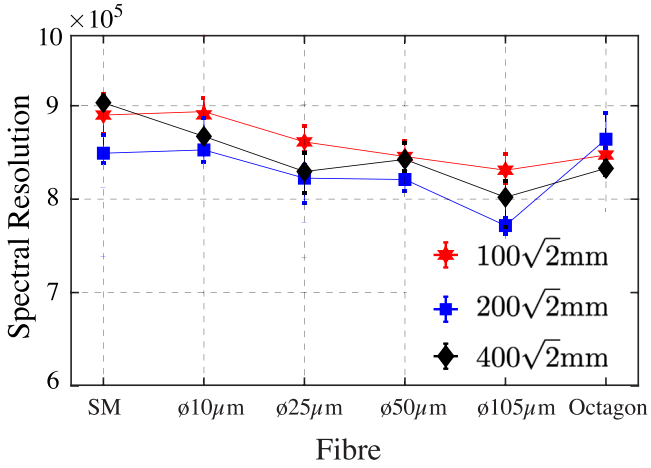

Figure 4. Spectral resolution with different kinds of input fiber and concave cylindrical mirrors of various focal lengths.

2014; Xu et al. 2017; Zhu et al. 2020) is used as an input signal to study the dispersion characteristics of the VIPA. The LFC modes are calibrated by an external cavity laser diode (LD) with a superior thermal stability ($\leqslant$100 MHz/°C) and a narrow line width ($<$100 kHz). The accurate wavelength of the LD can be read off from a high precision wavelength meter. The detailed calibration method can be found in Zhu et al. (2020).

In the experiments, the numerical aperture (NA) of the spectrograph system in the main dispersion direction is designed to be 0.25, which is larger than that of all the input fibers (the maximum is 0.22). In all of our experiments, a vibrator is attached to MMFs to provide the fiber with dynamic agitation. Small vibrations can excite more propagating modes supported by MMFs such that the speckle pattern on the exit face of the fibers is smoothed effectively and the modal noise is suppressed. Consequently, the intensities of comb teeth received by the CCD are more uniform, which makes the data reduction more accurate.

3.2. Spectral Resolution

Figure 3 shows the measured spectral resolutions for different kinds of input fibers, as well as the VIPA transmission efficiency quantified by the ratio of the comb intensities before and after the VIPA. It appears that the spectral resolution varies from the highest 8.97×10^5 with the SMF input to the lowest 7.62×10^5 with ∅105 μm MMF input in the same geometry, and diminishes slightly as the core diameter of the fiber increases, except for the OF. The spectral resolution of 8.10×10^5 with the OF input is higher than 8.00×10^5 of the ∅50 μm MMF input. The maximal transmission of 56.9% occurs in the case of the ∅25 μm MMF input. There are no significant differences in the transmission efficiencies between the SM and MM ∅105μm, which equal 43.5% and 41.7%, respectively.

The spectral resolution of VIPA spectrographs is insensitive to the core diameters of the input fibers, irrespective of the transmission efficiencies. The direct correlation between the spectral resolution and transmission efficiency is absent for various input fibers in our experiments, which demonstrates that the spectral resolution of a fiber-fed VIPA spectrograph is primarily determined by the characteristics of the VIPA, as described by Equation (12).

We attribute the lower resolution with larger core diameters of input fibers to the slight change in the geometry of the spectrograph. The size of the fiber core induces the change in the angle of incidence at the VIPA $\delta\theta_{\rm in}$, which makes the FWHM of the PSF increase by a factor of $\delta\theta_{\rm in}/\theta_{\rm in}$ (the analytical derivation is given in Section 3.4). Substituting the parameters of our spectrograph results in a 10.5% reduction in resolution with ∅105 μm MMF input compared to that with the SMF input. This is basically in agreement with our experimental results. In addition, the misalignment in the optical path and modal noises in MMFs frequently introduce additional errors. The OF has a better performance than the circular fibers (Ye et al. 2016) by suppressing the fiber modal noises, and therefore offers a higher spectral resolution even than that of the ∅50 μm MMF in the VIPA spectrograph.

We proceed to investigate the impacts of the source image size and the ray cone on the spectral resolutions by examining different focal lengths of the CL, as shown in Figure 4. The CLs are replaced by three concave cylindrical mirrors (CCMs) with focal lengths 400, 200, and 100 mm, giving rise to the effective focal lengths (EFLs) by a factor of $\sqrt{2}$. The experimental results reveal similar features, viz., (i) the spectrograph resolution is close to that of previous instruments, independent of the source size and the cone of the incident rays; and (ii) the spectral resolution decreases slightly as the core diameter of the input fibers increases, except for the OF. However, the source size together with the ray cone affect the diffraction envelope according to Equation (8), which will be discussed in more detail in the next section.

3.3. Diffraction Envelope

In a VIPA spectrograph, the length of one free spectral range (FSR) in the detector can be obtained from Equation (10), as follows

$$d_{\rm FSR} = \frac{\lambda \cdot F}{2t \tan\theta_{\rm in} \cos\theta}, \tag{13}$$

which is mainly determined by the focal length F of the OAPM and the thickness t of the VIPA. This length must fit the width of the diffraction envelope, which depends on the amplitude distribution $U_0(x)$ at the focal plane of CL. The Fourier transform indicates that the full width at half maximum

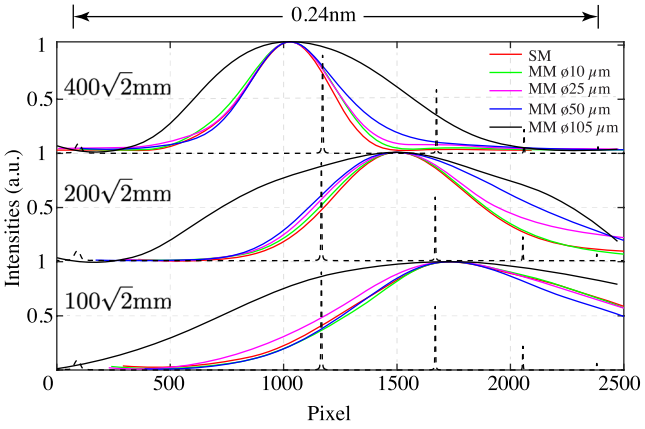

Figure 5. The diffraction envelopes with different kinds of input fibers and various focal lengths of concave cylindrical mirrors, as well as a LFC light source. The dashed lines indicate the FSRs of the VIPA corresponding to $\lambda = 760$ nm.

(FWHM) of diffraction envelope (Γ_D) is inversely proportional to that of $U_0(x)$. Figure 5 displays the profiles of the diffraction envelopes with different kinds of input fibers (SM & MMFs) and three focal lengths of CCMs (i.e., $f_{EFL} = 400\sqrt{2}$, $200\sqrt{2}$ and $100\sqrt{2}$ mm, respectively) with the same LFC light source as in the previous section. It is to be noted that all of the envelope profiles in the figures are an average result because neither the teeth of our LFC nor the LED is uniform in intensity. The inversely proportional dependence of the FHWM on the EFL of CCMs is unveiled unambiguously. By assuming a Gaussian distribution of $U_0^2(x)$, we obtain Γ_D with SMF inputs as 2.96 mm, 5.92 mm, and 11.84 mm for $f_{EFL} = 400\sqrt{2}$, $200\sqrt{2}$ and $100\sqrt{2}$ mm, respectively, which is basically consistent with the experimental results of 2.29 mm, 3.82 mm, and 7.59 mm. These deviations arise from the fact that the theoretical analysis is based on the diffraction-limited condition. In addition, all of the input MMFs demonstrate the analogous dependency that the diffraction envelope will be narrower when the image size at the focal plane of the CCM is larger.

Generally, the MMF input should possess a narrower diffraction envelope than that of SMF input in the same experimental condition, which is not the case in our experiments. In Figure 5, the profiles with $\varnothing \leqslant 50$ μm MMFs are very close to those of SMF in all three focal lengths, with the widest diffraction envelope from $\varnothing 105$ μm MMF input. This unconventional feature stems from the structured intensity distribution across the section of the MMF due to the coherence of the comb light resembling speckle patterns. We therefore record the images in the slit position, as shown in Figure 6, and investigate the intensity patterns in the exit sections of various input fibers. The yellow-dashed squares frame an identical area with a side length 9 μm, and the width of the yellow transverse stripes represents a slit size of 5 μm. The magnifications of all of the images are the same and the dimensions are calculated based on the mode field diameter (MFD) 5 μm of the SMF. In the experiments, the role of the vibrator is merely to excite more propagating modes and to smooth the speckle patterns over time instead of eliminating them. Figure 6 gives the typical sizes of the spots, which are similar in value for fibers with $\varnothing \leqslant 50$ μm. Whereas the $\varnothing 105$ μm MMF exhibits

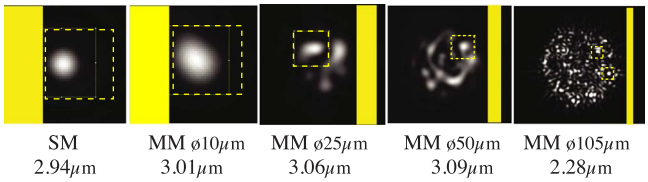

Figure 6. The intensity patterns with typical FWHMs on the sections of various input fibers.

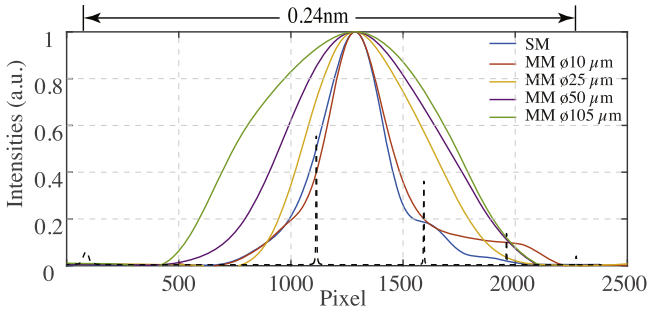

Figure 7. Diffraction envelopes with different kinds of input fibers. The light source is an LED. The dashed lines indicate the FSRs of the VIPA, corresponding to $\lambda = 760$ nm.

markedly smaller spots compared with the SMF and other MMFs. The speckle pattern of MMFs is composed of many such small spots, each of which acts as an independent light source in the multi-beam interference, thus forming the diffraction envelope. As a result, the $\varnothing 105$ μm MMF with smaller spots gives a wider diffraction envelope. It should be noted that the detailed speckle structure across the end of fibers always shifts, no matter how slowly the environmental condition changes. Therefore, the intensity patterns in Figure 6 were recorded at an instantaneous moment and do not exactly correspond to the situation in Figure 5.

Up to now, all of the sources that we have used are lasers that are coherent. When an incoherent light source, such as sunlight, is adopted, the theoretical calculations of the diffraction envelopes become a bit more complicated. Fortunately, these envelopes can be measured experimentally in a straightforward way. In our experiments, the incoherent light source obtained from the Thorlabs Light Emitting Diode (LED, M780F2) is led into the VIPA spectrograph. The measured FWHM of the diffraction envelopes is recorded in Figure 7 with $f_{SL2} = 50$ mm, $f_{CL} = 150$ mm and $f_{OAPM} = 100$ mm. The envelope width exhibits a distinct dependence of the diameter of input fibers from the case in which the laser source is employed. After removing the influences from the geometric parameters, such as f_{SL2}, f_{CL} and f_{OAPM}, we obtained the dependences of Γ_D and input fibers on the coherent (LFC, SLD) and incoherent (LED) sources for a more intuitive comparison, as shown in Figure 8. The envelope width increases approximately linearly with the core diameter of the input fibers when the source is incoherent, as indicated by the red circles, if the small difference between SMF and $\varnothing 10$ μm MMF is neglected, while for the coherent source it remains nearly unchanged until the core diameter reaches 50 μm, as indicated by the blue squares. Compared to the laser input, the LED exhibits a wider envelope with the $\varnothing 105$ μm MMF input. At present, the diffraction envelope of the VIPA can only be obtained from experiments and it deserves further study in the next step, both theoretically and experimentally. Some analysis

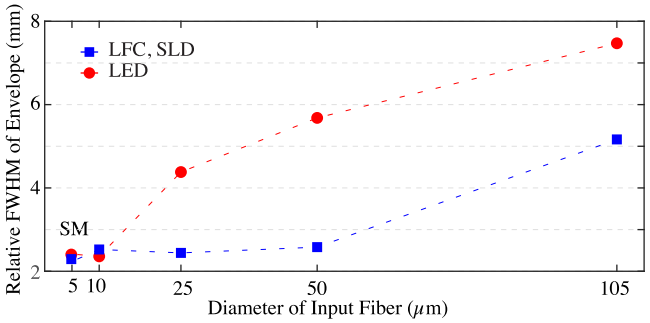

Figure 8. The relative FWHM of the diffraction envelope with coherent light sources (LFC, SLD) and incoherent light source (LED).

and discussion about the envelope characteristic of the VIPA comparing with traditional grating will be given in Section 4.

3.4. Point-spread Function (PSF)

Zhu et al. (2020) have revealed a feature of the VIPA spectrograph—namely, the FWHM of the PSF $\Gamma_{\rm PSF}$ varies gradually along the dispersion direction in contrast to the grating system. Here, we will study the PSF of the VIPA spectrograph in more detail, both theoretically and experimentally.

Equation (10) assumes an infinite dimension of the VIPA and infinite number of reflections. In our experiments, the actual number of reflections is about 163, due to the finite height 21 mm in the x-direction and the incident angle of 1°.6. The top panel of Figure 9 displays the analytical results from Equation (10) (dashed-red line) and numerical (dashed-blue line) PSF at $\lambda = 760.1535$ nm with $f_{\rm CL} = 400\sqrt{2}$ mm and $f_{\rm OAPM} = 516.8$ mm. The inset zooms in the framed region corresponds to the numerical $\Gamma_{\rm PSF} = 3.60$ pixels, which is larger than the analytical 2.45 pixels. To account for the aperture effects in the spectrograph, we need the Airy pattern given by

$$I_{\rm Airy} = \left(\frac{d^2}{4\lambda F}\right)^2 \left[\frac{J_1\left(\pi \frac{d}{\lambda F} u\right)}{\frac{d}{2\lambda F} u}\right]^2, \tag{14}$$

where J_1 is the first order Bessel function of the first kind and d is the diameter of the OAPM. The convolution of the PSF and the Airy pattern is respectively labeled by the solid red (analytical) and blue (numerical) lines, and the resultant FWHMs are both increased to 3.27 and 3.93 pixels, respectively (as shown in the inset).

According to Equation (10) , it is easy to see that the half maximum occurs at

$$\sin^2 \frac{\pi(\xi - \xi_0)}{\lambda_0} = \frac{1}{P} \tag{15}$$

for a given λ_0 with $\xi_0 = m_0 \cdot \lambda_0$. Then, the FWHM of ξ is given by

$$\Gamma_\xi = \frac{2\lambda_0}{\pi\sqrt{P}}, \tag{16}$$

where we have assumed that $\sin(\pi(\xi - \xi_0)/\lambda_0) = \pi(\xi - \xi_0)/\lambda_0$ for a small $\pi(\xi - \xi_0)/\lambda_0$. By plugging Equation (5) into

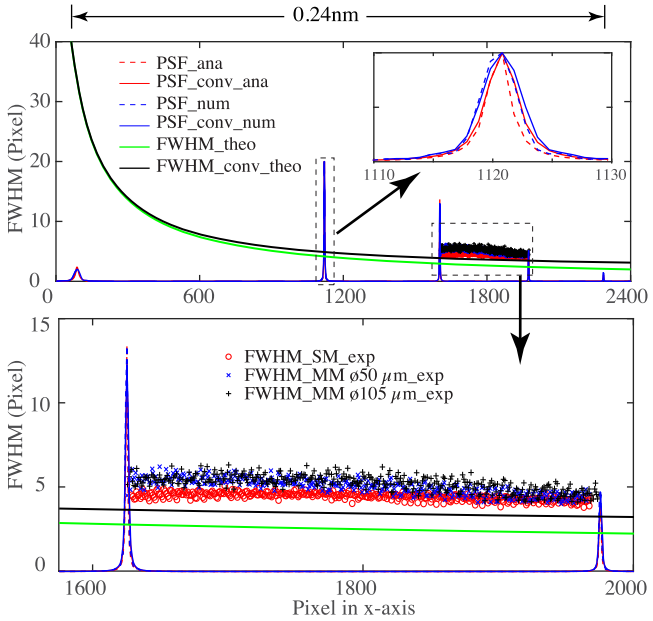

Figure 9. The distribution of FWHMs in the VIPA dispersion direction and analytical/numerical FWHMs with different kinds of input fibers.

Equation (16), we obtain $\Gamma_{\rm PSF}$ (the so-called resolution element) as

$$\Gamma_{\rm PSF} = \frac{2}{m_0\pi\sqrt{P}} \cdot \frac{\xi_0}{2n_r t\cos\theta_{\rm in} u/F^2 + 2t\tan\theta_{\rm in}\cos\theta/F}, \tag{17}$$

which is plotted in the top panel of Figure 9 by the solid green line.

To obtain the FWHM of the output pattern in the CCD, we approximate the Airy pattern by a Gaussian profile with the same FWHM $\Gamma_A = 1.029\lambda \cdot F/d$. The FWHM of the Voigt profile obtained from the convolution of the Lorentzian and the Gaussian ones can be calculated using the empirical formula (Olivero & Longbothum 1977)

$$\Gamma_v \approx 0.5346\Gamma_{\rm PSF} + \sqrt{0.2166\Gamma_{\rm PSF}^2 + \Gamma_A^2}, \tag{18}$$

which is shown in the top panel of Figure 9 with a solid black line. It is evident from these derivations that the PSF of VIPA spectrographs is well described by the Voigt profile, and the $\Gamma_{\rm PSF}$ is inversely proportional to the position.

We have conducted experiments with the parameters used in the above numerical simulations, and the Γ_v using SMF, ∅50, and 105 μm MMF inputs have been measured. The FWHMs in one FSR after data reduction are shown in the bottom panel of Figure 9. The experimental data follow a monotonic evolution and the averaged FWHMs of the three input fibers are 4.43, 5.02, and 5.22 pixels, respectively, which are all larger than the averaged theoretical result of ∼3.63 pixels. The differences in Γ_v between the experimental and theoretical results are reasonable because the numerical simulations are derived under the diffraction-limited condition.

Equation (17) also gives an analytical explanation that the bigger core diameter of the input MMF results in the lower spectral resolution of the VIPA spectrograph, as shown in Section 3.2. A small shift of the angle of incidence at the VIPA always causes a greater $\Gamma_{\rm PSF}$. The relative variation can be

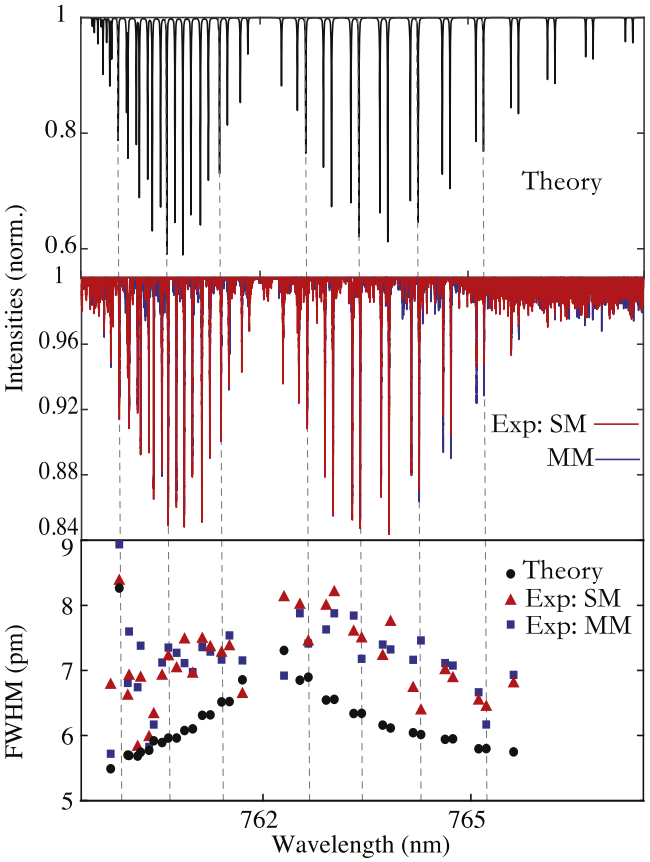

Figure 10. Top panel: the O_2 *A*-band spectra from the HITRAN 2020 database (Gordon et al. 2022). Middle panel: the O_2 *A*-band spectra measured with the VIPA spectrograph. Bottom panel: the FWHMs of the O_2 *A*-band absorption lines.

derived from Equation (17) as

$$\left(\frac{\delta\Gamma}{\Gamma}\right)_{\rm PSF} = \frac{\delta\theta_{\rm in}}{n_r u/F + \theta_{\rm in}}, \tag{19}$$

where $\theta_{\rm in}$ has been treated as a small quantity. The relative variation decreases with the position u on the detector, which is consistent with our experiment results in the bottom panel of Figure 9.

3.5. Verification via Oxygen Absorption Lines Measurements

To verify our results with a source similar to starlight from the telescope, we measured the oxygen *A*-band spectrum in the laboratory using our VIPA spectrograph with $\mathcal{R} \approx 8 \times 10^5$ as well as SMF and ∅105 μm MMF inputs. The spectrograph structure is the same as the one in Figure 3. A super-luminescent diode (Thorlabs, SLD770S) is used as a source and is first imported into an all-fiber, multi-pass, 3 m optical path Herriott gas cell, which is filled with oxygen at room temperature and an atmospheric pressure. The fiber-out SLD together with the LD are then coupled to the spectrograph simultaneously as the signal and the calibration source, respectively. Figure 10 shows the theoretical O_2 *A*-band spectrum calculated from HITRAN and the measured spectra with SMF and ∅105 μm MMF inputs. In total, 34 absorption lines (760 ∼ 766 nm) have been measured and their FWHMs in units of picometer are shown in the bottom panel. Based on the Lorentzian absorption line-shape and the spectrograph PSF, the average deviations from the theoretical FWHM are 0.916 and 0.975 pm, corresponding to the spectral resolution of $\mathcal{R} \approx 8.30 \times 10^5$ and 7.79×10^5 for SMF and ∅105 μm MMF inputs, respectively. These results are basically in agreement with the resolution measured by the LFC in Section 3.2.

The absorption depth—which is defined as $A_\nu \equiv (F_c - F_{\nu 0})/F_c$ with F_c and $F_{\nu 0}$, being, respectively, the flux density of the continuum background and the one at the center of the absorption line—is mainly affected by the intensity of the incident light in the experiments. The output spectrum of SLD770S is usually unstable over time and the fluctuations might dominate some absorption lines, particularly at long wavelengths 766 ∼ 770 nm. Consequently, the measured absorption depths between the SMF and MMF inputs are essentially different and not comparable.

4. Discussion and Conclusion

The most extensively used and successful instrument in astronomic observations is the échelle spectrograph, whose maximum resolution is depicted by

$$\mathcal{R}_{\rm max} = \frac{f_{\rm coll}}{w} \cdot 2\tan\beta, \tag{20}$$

where $f_{\rm coll}$ is the focal length of the collimated lens, w the diameter of the input slit or fiber, and β the grating's blaze angle. In astronomical spectrographs, all of these parameters depend on the telescope. To be specific, there is an inherent trade-off relationship between the spectral resolution of the échelle spectrograph and the telescope diameter (i.e., Pepe et al. 2000), as follows

$$\mathcal{R}_{\rm max} = \frac{h}{\phi D} \cdot 2\tan\beta, \tag{21}$$

where h is the size of the échelle grating in terms of the collimated beam diameter, ϕ is the field of view accepted by the fiber, and D the diameter of telescopes. The fundamental reason for this relationship is that the grating spectrograph is an imaging system whose PSF is the image of the input slit/fiber blurring on the detector. For a given telescope with a large diameter, the grating has to be large enough to attain a high spectral resolution because a reduction in the field of view ϕ will immediately cause a loss in the slit efficiency and the flux. Such an irreconcilable relationship restrains the further applications of the échelle spectrograph in larger telescopes.

Fortunately, the VIPA spectrograph as a non-imaging system can circumvent this difficulty. The width of input slit/fiber core diameter no longer matters for a high spectral resolution in the design of VIPA spectrographs and the resolution power is independent of the telescope itself. Thus, the size of the VIPA spectrograph can remain compact, irrespective of the diameters of telescopes, such that the manufacturing and operation costs are greatly reduced and the stability of the spectrograph is improved. For instance, the main dispersion element VIPA with a dimension of $22 \times 24 \times 1.68$ mm^3 is fully competent with a resolution of $\mathcal{R} \approx 4 \times 10^5$ to detect O_2 in the transmission spectrum of an Earth-like planet (Ben-Ami et al. 2018; López-Morales et al. 2019). Equipped with a high-efficiency volume phase holographic (VPH) transmission grating as the orthogonal dispersion element, the total volume

of the spectrograph can be below 0.05 m^3 (Zhu et al. 2020), which facilitates the control of temperature and pressure. Such a VIPA spectrograph can be applied to any telescope, regardless of its aperture.

The output efficiency of an échelle can be higher than 70%, and may be further improved by reducing stray light via optimized fabrication techniques and designs. Due to the losses of multiple reflections, the output efficiency of a VIPA has a transmission maximum (Weiner 2012; Zhu et al. 2020),

$$T_{\max} = \frac{1 - |r_2|^2}{1 - |r_1|^2|r_2|^2}, \tag{22}$$

which highly relies on the reflectivity $|r_1|^2$ of the coating on the front side of the VIPA. When $|r_2|^2 = 95\%$, $T_{\max}$ reaches above 91.3% with $|r_1|^2 = 99.5\%$ and even 98.1% for $|r_1|^2 = 99.9\%$. In fact, such coatings are already available with current technologies. Meanwhile, a lower partial reflectivity coating on the rear side can also enhance the total transmission efficiency at a cost of a diminished resolution power. The actual transmission is sensitive to the number of light reflections, which is further determined by the dimension of the VIPA in the dispersion direction and the angle of incidence. In addition, the coupling efficiency of space light into the VIPA must also be considered, and therefore the spectrograph's geometrics, such as the opening angle and the focal spot size of the light beam, should be designed carefully.

For a grating-based spectrograph, the blaze function modulates the interference function, which can be considered as the diffraction envelope generated by light coming from a single groove of the grating. For échelle, the length of one FSR $d_{\mathrm{FSR\_g}}$ in the detector is always slightly less than the width of the blazed function due to its facet characteristics. In the case of the VIPA spectrograph, the relationship between the two parameters is no longer valid. According to Equation (13), the VIPA FSR in the detector is predominantly dependent on the focal length of the lens in front of the detector. Moreover, experiments have shown that the image size and coherence of sources determine the diffraction envelope of a VIPA, so that the relation between the FSR and the envelope width has to be guaranteed with the help of theoretical analysis and experimental measurements.

In practice, the PSF of a spectrograph is rather crucial for the data reduction and analysis. Many scientists have made great efforts to pursue a more accurate method of spectral extraction to limit of photon noise and native instrumental resolution (Bolton & Schlegel 2010; Wang et al. 2016; Hao et al. 2018; Kos et al. 2018). Theoretically, the PSF of a VIPA spectrograph is approximated by a Voigt function, compared with the sinc-squared function in the échelle spectrograph. Furthermore, Γ_{PSF} also varies in the dispersion direction and is affected by the size of the detector due to the off-axis aberration. The PSF of a VIPA spectrograph is therefore more complicated than that of an échelle spectrograph. By now, the work on spectral extraction of a VIPA spectrograph is very limited and deserves further investigation, particularly in astronomical observations.

The VIPA spectrograph is a promising instrument to attain an ultra-high spectral resolution ($\mathcal{R} > 3 \times 10^5$) on very large telescopes. At lower resolution ($10^5 \sim 3 \times 10^5$), the shorter FSR of a VIPA compared to an échelle of equivalent spectral resolution creates a challenge for detection when observing a wider spectral range, especially in visual light. In addition, a thin VIPA (thickness $t < 1$ mm) would make it difficult to maintain a high coupling efficiency with MMF inputs. We are currently focusing on these issues and are trying to solve them in the next step.

In conclusion, we have studied and compared the dispersion characteristics of the VIPA spectrograph working in the diffraction- and seeing-limited conditions, including the spectral resolution, the diffraction envelope, and its point-spread function. To design a VIPA spectrograph on large telescopes, various aspects should be taken into account. We found that the spectral resolution is independent of the diffraction- or seeing-limited conditions, while the diffraction envelope associates closely with the coherence of light source and the PSF is inversely proportional to the spatial position on the detector.

The authors acknowledge support from the National Natural Science Foundation of China (grant Nos. 11973009 and 11933005). J.H. thanks the CAS Pioneer Hundred Talents Program. The authors also thank Prof. Zhigang Zhang (PKU) for providing high-repetition-rate LFC technology.

ORCID iDs

Xiaoming Zhu https://orcid.org/0000-0003-1088-1457
Jinping He https://orcid.org/0000-0002-1899-3384

References

Anglada-Escudé, G., Amado, P. J., Barnes, J., et al. 2016, Natur, 536, 437
Bailén, F. J., Suárez, D. O., & del Toro Iniesta, J. 2019, ApJS, 241, 9
Bechter, A., Crass, J., Ketterer, R., et al. 2016, Proc. SPIE, 9909, 903
Ben-Ami, S., López-Morales, M., Garcia-Mejia, J., Abad, G. G., & Szentgyorgyi, A. 2018, ApJ, 861, 79
Bolton, A. S., & Schlegel, D. J. 2010, PASP, 122, 248
Bourdarot, G., Le Coarer, E., Bonfils, X., et al. 2017, CEAS, 9, 411
Bourdarot, G., Le Coarer, E., Mouillet, D., et al. 2018, Proc. SPIE, 10702, 107025Y
Carlotti, A., Bidot, A., Mouillet, D., et al. 2022, Proc. SPIE, 12184, 523
Conconi, P., Riva, M., Pepe, F., et al. 2013, Proc. SPIE, 8842, 178
Crepp, J. R., Crass, J., King, D., et al. 2016, Proc. SPIE, 9908, 346
Diddams, S. A., Hollberg, L., & Mbele, V. 2007, Natur, 445, 627
Erskine, D. J., Edelstein, J., Wishnow, E. H., et al. 2016, JATIS, 2, 025004
Fiore, A., Zhang, J., Shao, P., Yun, S. H., & Scarcelli, G. 2016, ApPhL, 108, 203701
Gordon, I., Rothman, L., Hill, C., et al. 2022, JQSRT, 277, 107949
Hao, Z., Ye, H., Han, J., et al. 2018, PASP, 130, 125001
Hu, X., Sun, Q., Li, J., et al. 2015, OExpr, 23, 1
Jiang, T., Wang, A., Wang, G., et al. 2014, OExpr, 22, 1835
Jovanovic, N., Cvetojevic, N., Schwab, C., et al. 2016, Proc. SPIE, 9908, 196
Knauth, D. C., Federman, S., & Lambert, D. L. 2003, ApJ, 586, 268
Kos, J., Bland-Hawthorn, J., Betters, C. H., et al. 2018, MNRAS, 480, 5475
Lauroesch, J., Meyer, D. M., & Blades, J. 2000, ApJL, 543, L43
2020, LightMachinery Inc.www.lightmachinery.com
López-Morales, M., Currie, T., Teske, J., et al. 2019, arXiv:1903.09523
Monroe, T. R., Meléndez, J., Ramírez, I., et al. 2013, ApJL, 774, L32
Muirhead, P. S., Edelstein, J., Erskine, D. J., et al. 2011, PASP, 123, 709
Olivero, J. J., & Longbothum, R. 1977, JQSRT, 17, 233
Pepe, F., Mayor, M., Delabre, B., et al. 2000, Proc. SPIE, 4008, 582
Schroeder, D. 2000, Astronomical Optics (Cambridge, MA: Academic Press), 314
Seifahrt, A., Stürmer, J., & Bean, J. L. 2016, Proc. SPIE, 9912, 590
Shirasaki, M. 1996, OptL, 21, 366
Wang, L., Grupp, F., Kellermann, H., et al. 2016, Proc. SPIE, 9913, 1311
Weiner, A. M. 2012, ApOpt, 51, 8187
Xiao, S., Weiner, A. M., & Lin, C. 2004, IJQE, 40, 420
Xu, B., Yasui, H., Nakajima, Y., et al. 2017, OExpr, 25, 11910
Ye, H., Han, J., Wu, Y., & Xiao, D. 2016, Proc. SPIE, 9908, 99087E
Zhu, X., Lin, D., Hao, Z., Wang, L., & He, J. 2020, AJ, 160, 135